Modelling study on the three-dimensional neutron depolarisation response of the evolving ferrite particle size distribution during the austenite–ferrite phase transformation in steels

Fang, H.; van der Zwaag, S.; van Dijk, N. H.

DOI
10.1080/14786435.2018.1465239

Publication date
2018

Document Version
Final published version

Published in
Philosophical Magazine

Philosophical Magazine

ISSN: 1478-6435 (Print) 1478-6443 (Online) Journal homepage: http://www.tandfonline.com/loi/tphm20

Modelling study on the three-dimensional neutron depolarisation response of the evolving ferrite particle size distribution during the austenite–ferrite phase transformation in steels

H. Fang, S. van der Zwaag & N. H. van Dijk

To cite this article: H. Fang, S. van der Zwaag & N. H. van Dijk (2018): Modelling study on the three-dimensional neutron depolarisation response of the evolving ferrite particle size distribution during the austenite–ferrite phase transformation in steels, Philosophical Magazine, DOI: 10.1080/14786435.2018.1465239

To link to this article: https://doi.org/10.1080/14786435.2018.1465239

Published online: 23 Apr 2018.

PHILOSOPHICAL MAGAZINE, 2018
https://doi.org/10.1080/14786435.2018.1465239

Taylor & Francis
Taylor & Francis Group

Modelling study on the three-dimensional neutron depolarisation response of the evolving ferrite particle size distribution during the austenite–ferrite phase transformation in steels

H. Fang[a,b], S. van der Zwaag[b,c] and N. H. van Dijk[a]

[a]Faculty of Applied Sciences, Fundamental Aspects of Materials and Energy Group, Delft University of Technology, Delft, The Netherlands; [b]Faculty of Aerospace Engineering, Novel Aerospace Materials Group, Delft University of Technology, Delft, The Netherlands; [c]School of Materials Science and Engineering, Tsinghua University, Beijing, China

ABSTRACT

The magnetic configuration of a ferromagnetic system with mono-disperse and poly-disperse distribution of magnetic particles with inter-particle interactions has been computed. The analysis is general in nature and applies to all systems containing magnetically interacting particles in a non-magnetic matrix, but has been applied to steel microstructures, consisting of a paramagnetic austenite phase and a ferromagnetic ferrite phase, as formed during the austenite-to-ferrite phase transformation in low-alloyed steels. The characteristics of the computational microstructures are linked to the correlation function and determinant of depolarisation matrix, which can be experimentally obtained in three-dimensional neutron depolarisation (3DND). By tuning the parameters in the model used to generate the microstructure, we studied the effect of the (magnetic) particle size distribution on the 3DND parameters. It is found that the magnetic particle size derived from 3DND data matches the microstructural grain size over a wide range of volume fractions and grain size distributions. A relationship between the correlation function and the relative width of the particle size distribution was proposed to accurately account for the width of the size distribution. This evaluation shows that 3DND experiments can provide unique *in situ* information on the austenite-to-ferrite phase transformation in steels.

ARTICLE HISTORY
Received 21 December 2017
Accepted 2 April 2018

KEYWORDS
Neutron scattering; steel; phase transformation; grain size distribution; magnetisation

1. Introduction

Three-dimensional neutron depolarisation (3DND) is a powerful technique to characterise the magnetic microstructure of polycrystalline bulk materials on the

CONTACT H. Fang H.Fang@tudelft.nl

(sub)micron scale [1–3]. In such measurements, a polarised neutron beam interacts with the local magnetic induction in a magnetised sample, which results in a change of the polarisation vector of the neutron beam upon transmission through the (magnetised) sample. This change in polarisation is characterised by a rotation angle and by a shortening of the polarisation vector with respect to the initial polarisation. The mean magnetisation causes a net rotation of the polarisation vector and the magnetic inhomogeneities result in a decrease in polarisation. For a sample containing ferromagnetic particles (grains) in a paramagnetic matrix, the rotation angle monitors the phase fraction of the ferromagnetic phase inside the sample. The shortening of the polarisation determines magnetic correlation length, and thereby a mean magnetic particle (grain) size along the neutron beam.

This technique has successfully been used to study static and dynamic properties of magnetic microstructures in a wide range of materials such as magnetic recording materials, superconductors, amorphous metals and steels [4–9]. In low-alloyed steels, the austenite-to-ferrite [10] and the austenite-to-pearlite [11] phase transformations have been studied using *in situ* 3DND measurements. In such steels, the high temperature austenite phase, which has an *fcc* lattice structure and is paramagnetic, transforms into ferrite with a *bcc* structure below a characteristic transformation temperature (A_3). Below the Curie temperature T_C (=1043 K for pure Fe), the equiaxed ferritic phase becomes ferromagnetic. At a transformation temperature below the so-called A_1 temperature, the remaining austenite, being enriched in carbon, transforms into a lamellar structure composed of ferrite and cementite Fe_3C plates, the so-called pearlite. In this study, we focus on the microstructure evolution for a two-phase austenite–ferrite mixture, in which the equiaxed austenite grains form the continuous parent phase and the equiaxed ferrite grains are the emerging product phase.

Key parameters to characterise the microstructure evolution during the austenite-to-ferrite transformation in steels for this magnetically inhomogeneous ferromagnetic system are the ferritic volume fraction and the ferritic particle size. Rosman and Rekveldt [1] derived the theoretical framework for the determination of the magnetic phase fraction and the (spherical) particle size in the case of monodisperse ferromagnetic particles in a dilute non-magnetic medium from neutron depolarisation experiments. Te Velthuis and co-workers [12] investigated the magnetic particle size obtained by neutron depolarisation and compared it to the ferrite grain size using a numerical model. The results showed that the magnetic particle size calculated from the neutron depolarisation is in good agreement (within of 10–20%) with the actual average ferrite grain size. Simultaneous measurements of the (magnetic) volume fraction and the average (magnetic) particle size by *in situ* neutron depolarisation measurements provide unique insight in the austenite-to-ferrite transformation in steels, as it is one of the few physical characterisation techniques known to determine both the volume fraction and the average particle size on a micron length scale in a single experiment. Such information makes it possible to separate nucleation and growth effects during

the solid-state phase transformation and to reconstruct important details of the progression of this important solid-state phase transformation. However, the analysis of the 3DND data has not yet been brought to a level that makes it possible to capture not only the average ferritic particle size but also the width of the particle size distribution. The ferrite grain size distribution holds even more detailed information on the ferrite grain nucleation and growth rate and this information is crucial for accurate modelling of the austenite decomposition in low-alloyed steels during cooling. It is the aim of the present work to extend the 3DND data analysis in this direction.

To investigate the influence of the particle size distribution on the interpretation of 3DND data, we developed a model to compute the magnetic configuration for a given 3D microstructure. From this microstructure, the 3DND parameters were derived. By tuning the phase transformation parameters, the microstructure can be varied. We thereby investigated the effect of size distribution on the particle size derived from the 3DND analysis by a comparison to the mean particle size of the actual distribution. This theoretic study provides the foundation for the 3DND analysis of evolving ferromagnetic microstructures starting from a fully paramagnetic parent phase.

2. Neutron depolarisation

Two approaches have been developed to describe the neutron depolarisation due to the interaction of a polarised neutron beam with a collection of magnetic particles: (i) the Larmor and (ii) the scattering approach. Rosman and Rekveldt [13] found that both approaches are fully equivalent as long as all scattered neutrons enter the analyser during the measurement. Here, we will just briefly present the neutron depolarisation in Larmor approach. A detailed overview of the neutron depolarisation theory can be found elsewhere [1,2,7,13].

As shown in Figure 1, the neutron depolarisation technique measures the change of the polarisation for a polarised neutron beam after transmission through a magnetic material. The relationship between the initial polarisation vector ($\vec{P}^0$) and the polarisation vector after transmission ($\vec{P}'$) can be expressed as $\vec{P}' = \hat{D}\vec{P}^0$, where $\hat{D}$ is a depolarisation matrix that contains 3 × 3 elements. Generally, the depolarisation matrix can be expressed in terms of a rotation of the beam polarisation and a reduction in beam polarisation (described by a matrix $\hat{D}'$) [1,2]. This reduction in beam polarisation is directly related to the field correlation matrix $\hat{\alpha}$ of the sample volume V_W with components α_{ij} ($i, j = x, y$ or z) :

$$\alpha_{ij} = \frac{1}{V_w} \int_{V_w} d^3\vec{r} \int_0^x \Delta B_i(x,y,z)\,\Delta B_j(x',y,z)\,dx' \tag{1}$$

where $\vec{r} = (x,y,z)$ is a spatial vector, 0 is the position where neutrons enter the sample, (x, y, z) and (x', y, z) are two different arbitrary points in the sample

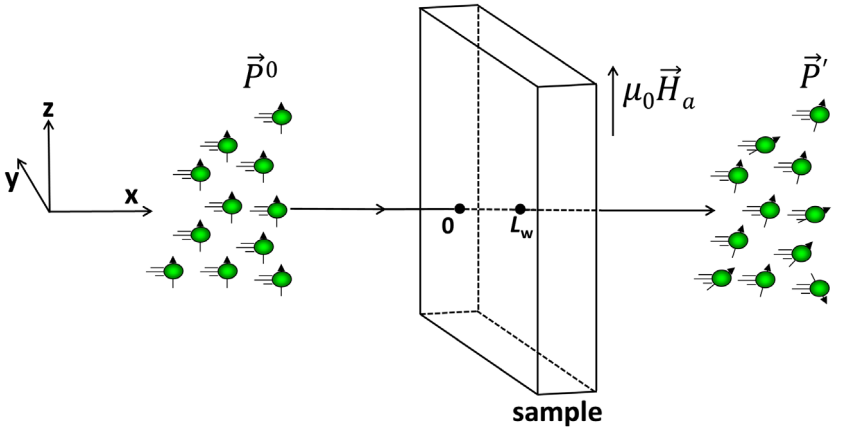

Figure 1. (colour online) Sketch of the neutron depolarisation method shows that a polarised neutron beam ($\vec{P}^0$) is partly depolarised ($\vec{P}'$) after transmitting through a magnetised sample subjected to an external applied magnetic field $\mu_0\vec{H}_a$ along *z* direction.
Note: The positions where neutrons enter and leave the sample are denoted as 0 and L_w, respectively. The sample volume is V_w.

volume and $\Delta B_i(\vec{r})$ is the *i*-component of $\Delta\vec{B}(\vec{r})$ that corresponds to the variation in magnetic induction with the mean magnetic induction $\langle\vec{B}\rangle$ expressed as $\Delta\vec{B}(\vec{r}) = \vec{B}(\vec{r}) - \langle\vec{B}\rangle$ (see Figure 1 for the coordinate system). In the absence of correlations between the variations in the field components $\Delta B_i(\vec{r})$ and $\Delta B_j(\vec{r})$ $(i \neq j)$ along the neutron path, this correlation matrix $\hat{\alpha}$ is diagonal. The correlation function ξ, which is proportional to the correlation length of $|\Delta\vec{B}(\vec{r})|^2$ along the neutron beam, can be expressed as

$$\xi = \sum_i \alpha_{ii} \tag{2}$$

In the absence of a net polarisation rotation, the elements of the correlation matrix $\hat{\alpha}$ and the depolarisation matrix $\hat{D}'$ are related as:

$$D'_{ij} = \delta_{ij}\left(1 - c_1 L_w \xi\right) + c_1 L_w \alpha_{ij} \tag{3}$$

where δ_{ij} is the Kronecker delta, $c_1 = 2.15 \times 10^{29}\lambda^2\ T^{-2}\ \mathrm{m}^{-4}$ with λ the neutron wavelength and L_w is the sample length along the neutron beam. Rosman and Rekveldt [13] showed that in the Fourier space, $\hat{\alpha}$ is directly related to the magnetisation of the sample $\vec{M}(\vec{r})$:

$$\alpha_{ij} = \frac{8\pi^4}{V_w}\int_S B_i(\vec{s})B_j(-\vec{s})d^2\vec{s} - \frac{L_w}{2}\langle B_i\rangle\langle B_j\rangle \tag{4}$$

where $\vec{B}(\vec{s}) = \frac{\mu_0}{(2\pi)^3}\int_V \left(\tilde{s}\times\left[\vec{M}(\vec{r})\times\tilde{s}\right]\right)e^{i\vec{s}\cdot\vec{r}}d^3\vec{r}$, μ_0 is the permeability of vacuum, $\vec{s}$ is the reciprocal lattice vector and $\tilde{s} = \vec{s}/|\vec{s}|$ its unit vector. As described in Ref.

[12], for a distribution of uncorrelated ferromagnetic particles, the diagonal elements of the matrix $\hat{\alpha}$ have the following analytical solutions:

$$\alpha_{xx} = f\left(\mu_0 M_s\right)^2 \left(\frac{6\langle m_x^2 \rangle \langle R^4 \rangle}{8\langle R^3 \rangle} - \frac{2}{3} c_2 \langle m_x \rangle^2 \langle R^3 \rangle^{\frac{1}{3}} \right) \tag{5}$$

$$\alpha_{yy} = f\left(\mu_0 M_s\right)^2 \left(\frac{3\left(\frac{3}{4}\langle m_y^2 \rangle + \frac{1}{4}\langle m_z^2 \rangle\right)\langle R^4 \rangle}{8\langle R^3 \rangle} - \frac{2}{3} c_2 \langle m_y \rangle^2 \langle R^3 \rangle^{\frac{1}{3}} \right) \tag{6}$$

$$\alpha_{zz} = f\left(\mu_0 M_s\right)^2 \left(\frac{3\left(\frac{1}{4}\langle m_y^2 \rangle + \frac{3}{4}\langle m_z^2 \rangle\right)\langle R^4 \rangle}{8\langle R^3 \rangle} - \frac{2}{3} c_2 \langle m_z \rangle^2 \langle R^3 \rangle^{\frac{1}{3}} \right) \tag{7}$$

where f is the volume fraction of the ferromagnetic phase, $\vec{m} = \vec{M}/M_s$ is the reduced magnetisation scaled to the saturation magnetisation M_s of the ferromagnetic phase, $c_2 = \left(4\pi f^2/81\right)^{1/3}$ is a constant and R is the radius of the ferromagnetic particle. According to Equation (2), the correlation function ξ then corresponds to

$$\xi = \frac{2f\left(\mu_0 M_s\right)^2}{3c_3} \frac{\langle R^4 \rangle}{\langle R^3 \rangle} \left(1 - c_2 c_3 m^2 \frac{\langle R^3 \rangle^{\frac{4}{3}}}{\langle R^4 \rangle} \right) \tag{8}$$

where $m = \left|\vec{m}\right|$ and c_3 is a constant that depends on the shape, orientation and spatial distribution of the ferromagnetic particles. For identical spheres, this constant is $c_3 = 16/\left[9\left(1 + \langle m_x^2 \rangle\right)\right]$. Equation (8) shows that ξ depends on the ratio of the higher order averages of the particle sizes, which suggests that ξ includes the information of both the average particle radius $\langle R \rangle$ and the spread in radius. By writing $\delta = \frac{\langle R^4 \rangle}{\langle R^3 \rangle}$ and assuming $\frac{\langle R^3 \rangle^{\frac{4}{3}}}{\langle R^4 \rangle} \to 1$, Equation (8) is transformed to give the relationship between δ and ξ:

$$\delta = \frac{3c_3\xi}{2f\left(\mu_0 M_s\right)^2\left(1 - c_2 c_3 m^2\right)} \tag{9}$$

These equations show that one can derive the neutron depolarisation parameters $\hat{\alpha}$, ξ and $\hat{D}$ by computing the orientation of the magnetic moments for all magnetic particles in a particulate system. Furthermore, the characteristic particle size δ can be obtained with Equation (9) from the magnetic correlation length. In a 3DND measurement, one measures the transmission of the polarisation components to

derive the depolarisation matrix $\hat{D}$ and then calculate f and δ [10,11]. However, it should be noted that several approximations have been made in the derivation of Equation (9). The goal of the present work is to evaluate how the particle size distribution influences the analysis of the neutron depolarisation data and how large the potential deviations are for our system of interest in the case of ferrous phase transformations.

3. Microstructural magnetic model

The present model was developed on the basis of the austenite–ferrite microstructural model by Te Velthuis and co-workers [12] in which spherical (ferromagnetic) ferritic particles nucleate and grow in a fully (paramagnetic) austenitic microstructure that is generated by a Voronoi construction. A given 3D microstructure with a preset ferrite size distribution was generated first and its magnetic configuration was computed. The resulting 3DND characteristics were then calculated using Equations (4)–(7). After the 3DND parameters were obtained, Equation (9) was used to back calculate the magnetic particle size, which should be identical to the given particle size if all the used approximations are valid. Otherwise, a deviation will be generated, which can be evaluated subsequently. The present work is generic in nature, but has been applied to the magnetic microstructure evolution during the austenite–ferrite phase transformation in steels. In this phase transformation, the high-temperature austenite phase is nonmagnetic (paramagnetic), while the low-temperature ferrite phase is magnetic (ferromagnetic) below the Curie temperature T_C [10–12].

To start the simulations, a 3D microstructure comprising a nonmagnetic phase and a magnetic phase was created in a cubic box with a length L_b. The magnetic particles are assumed to be spherical and centred at the grain corners of the nonmagnetic phase, as discussed in [14]. For the austenite–ferrite microstructure in low-alloyed steels, the parent austenite grain corners, edges and surface are the preferred nucleation sites for the ferrite particles [15]. For isothermal transformations at a low undercooling or for transformations at a slow continuous cooling, austenitic grain corners are the most probable sites for the nucleation of ferrites [16,17]. The geometry of the ferrite particles depends largely on the specific transformation conditions. Although ferrite can grow into allotriomorphic plate-like particles along grain boundaries [18–20], most experimental [17] and modelling [21,22] studies showed relatively isotropic equiaxed ferrite in the early stages of the phase transformation when coalesce of particles has not yet appeared. In the present modelling, the geometry of the magnetic particles has been simplified to a spherical shape as this shape is close to the most frequently observed equiaxed ferrite particles. The collection of the magnetic particles closely resembles a log-normal size distribution. Each magnetic particle is then assigned with a radius, a spatial location and a randomly chosen magnetic anisotropy (referred to as the *easy axis*). The magnetisation of each magnetic particle $\vec{M} = M_s\vec{m}$ is assumed to

be homogeneous with a magnitude M_s and an orientation $\vec{m}$. The orientation for each magnetic particle was computed by extending the original Stoner–Wohlfarth model [23] to include the mean field and the magnetic interaction with neighbouring particles. To compute the magnetic configuration, the total energy of all magnetic particles is minimised.

For a domain i, the local field $\vec{H}_{l,i}$ is the summation of the applied field $\vec{H}_a$, the total magnetic dipole field $\sum \vec{H}_{d,ji}$ (sum over j) and the mean field $\alpha\vec{M}$:

$$\vec{H}_{l,i} = \vec{H}_a + \sum \vec{H}_{d,ji} + \alpha\vec{M} \tag{10}$$

where α is the mean field parameter [24], which has a fixed value of $\alpha = 1/3$ in the present study. The magnetic dipole field accounts for the total field originating from all neighbouring magnetic particles [25]. The dipole field for particle i from another particle j is expressed as

$$\vec{H}_{d,ij} = \frac{1}{4\pi} \frac{3\hat{r}_{ji}\left(\hat{r}_{ji} \cdot \vec{M}_j\right) - \vec{M}_j}{\left|\vec{r}_{ji}\right|^3} V_j \tag{11}$$

where $\vec{r}_{ji}$ is the displacement vector from particle j to i, $\vec{M}_j$ is the magnetisation and V_j is the volume of particle j. When the magnitude of the dipole field $H_{d,ij}$ (which depends on r_{ij} and V_j) becomes smaller than 0.5% M_s, it is considered to be negligible and is ignored in the calculations. This threshold corresponds to: $r_{ij}/(3V_j/4\pi)^{1/3} > 5.2$.

The magnetic energy E_i of a particle i is the sum of the magnetostatic energy $E_{H,i}$ and the anisotropy energy $E_{a,i}$

$$E_i = E_{H,i} + E_{a,i} \tag{12}$$

with $E_{H,i} = -\mu_0 H_{l,i} M_s cos\varphi_i$ and $E_{a,i} = \frac{1}{2}\mu_0 N_s M_s^2 \sin^2\left(\theta_i - \varphi_i\right)$, where φ_i is the angle between $\vec{H}_{l,i}$ and $\vec{M}_j$, θ_i is the angle between $\vec{H}_{l,i}$ and the easy axis and N_s is the shape anisotropy factor, chosen to be $N_s = 0.1$ to reflect the sample geometries used in the ND experiments. To derive the minimum of E_i expressed in Equation (12), one can get a unique solution for φ_i by applying the constraints $\frac{dE_i}{d\varphi_i} = 0$ and $\frac{d^2E_i}{d\varphi_i^2} > 0$ [26]. Once the minimum energy is derived for all particles, the total energy of the whole system is calculated and compared to the one derived in the previous calculation until the difference between them is less than 0.5%. By this iterative process, a stable magnetic configuration can be achieved. The mean magnetisation $\langle\vec{M}\rangle$, the reduced magnetisation m and the values of $\langle m_i^2\rangle$ are calculated in the same way as in [12].

The 3DND parameters are then calculated as a function of applied magnetic field from the computed magnetic configuration. The magnetic particle size δ_{ND} is estimated from the 3DND data with Equation (9) and compared to the known structural particle size δ_s derived from the computed magnetic microstructure.

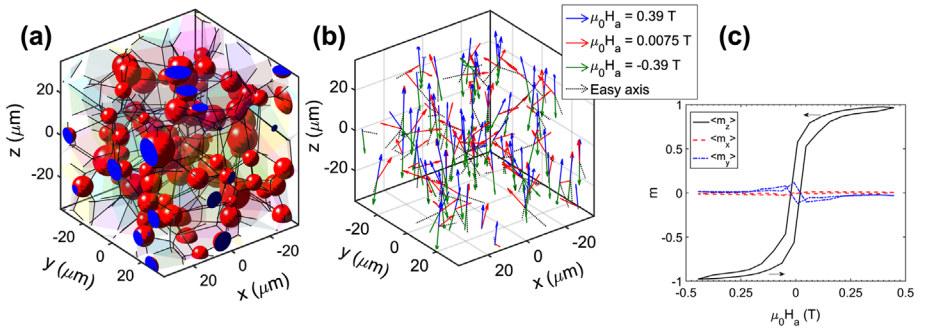

Figure 2. (colour online) (a) 3D visualisation of the microstructure with $f = 0.10$, $\rho_\alpha = 2.45 \times 10^{14}\,\mathrm{m}^{-3}$, $\langle R \rangle = 4.4$ μm and $\sigma/R = 0.25$ and (b) the computed magnetisation for each particle illustrated by the orientation of the arrows with easy axis shown in dashed lines. (c) The calculated $<m_x>$, $<m_y>$ and $<m_z>$ as a function of the applied field (arrows indicate the changing direction of applied field) for a magnetic hysteresis loop.

To study the influence of grain size distribution, computations are carried out for a series of given microstructures, composed of (paramagnetic) austenite and (ferromagnetic) ferrite, that evolved as a function of temperature [14]. The saturation magnetisation of ferrite M_s is calculated with the formula proposed by Arrott and Heinrich [27]. The starting austenite structure is generated in a cubic box with $L_b = 70$ μm containing quasi-isotropic austenite grain cells with an average diameter of $d_\gamma = 20$ μm and a minimum value of $d_{min} = 12$ μm constructed via a conventional Voronoi construction method. The ferrite is generated at the corners of the austenite grains and allowed to grow isotropically once nucleated, resulting in a ferrite grain number density ρ_α, volume fraction f, average grain radius $\langle R \rangle$ and a standard deviation σ. The ferrite grain size distribution is produced in such a way that both f and $\langle R \rangle$ are kept constant, whilst ρ_α is adjusted to ensure a constant ratio of $\sigma/\langle R \rangle$.

4. Results and discussion

4.1. Influence of the size distribution

Figure 2(a) shows the microstructure generated for $f = 0.10$, $\rho_\alpha = 2.45 \times 10^{14}\,\mathrm{m}^{-3}$, $R = 4.4$ μm and $\sigma/R = 0.25$ and the corresponding magnetisation for each particle. By representing the particles by magnetic dipoles (of strength $VM_s\vec{m}$ with V the volume of the particle) located at their centres, we can directly visualise the orientations of the magnetisation for each particle at different applied fields, as shown in Figure 2(b).

At a positive field of $\mu_0 H_a = 0.39\ T$, the $\vec{M}$ of all particles tend to incline towards the direction of the applied field. However, due to the magnetic interactions of the particles, the local magnetisation inside the particles is not perfectly aligned, which results in $<m_z> = 0.97$ (with $<m_x> \approx <m_y> \approx 0$). When $\mu_0 H_a$ decreases to

Table 1. The configuration of the ferrite microstructure at an identical magnetic fraction.

f	ρ_a ($\times 10^{14}$ m^{-3})	R (μm)	$\sigma\langle R\rangle$
0.10	2.80	4.4	0
0.10	2.45	4.4	0.25
0.10	1.75	4.4	0.50

0.0075 T, the local magnetisation shows more orientational disorder resulting in $<m_z>$ = 0.57. When $\mu_0 H_a$ is reversed to −0.39 T, most magnetisation vectors rotate to align with the negative applied field. As shown in Figure 2(c), the overall change in magnetisation shows a magnetic hysteresis loop. As in the actual 3DND experiment, the magnetic field is aligned along the z-axis the magnitude of $<m_x>$ and $<m_y>$ is expected to be very small. We will therefore only focus on $<m_z>$ in the remainder of the analysis.

The first calculation was done for different microstructures with a fixed magnetic fraction f. Table 1 gives the configuration of the magnetic microstructure with $f = 0.10$ for different values of $\sigma/\langle R\rangle$. Figure 3 shows the characteristic 3DND parameters: the rotation angle φ, the determinant of depolarisation matrix $\det(\hat{D})$, the correlation function ξ and the particle radius δ_{ND} as a function of the applied field. By increasing $\sigma/\langle R\rangle$ from 0 to 0.25, the curves for φ hardly change. Only when $\sigma/\langle R\rangle$ is increased to 0.50, the hysteresis increases and the saturation levels decreases. The value of $\det(\hat{D})$ is more sensitive to σ/R as it probes the variations in local magnetic induction. As shown in Figure 3(b), the magnitude of $\det(\hat{D})$ decreases with increasing $\sigma/\langle R\rangle$. This indicates that for identical values of f and $\langle R\rangle$, the polarisation is reduced more strongly when the spread in size distribution increases. The lowest values for $\det(\hat{D})$ are observed for the smallest applied fields ($|\mu_0 H_a| < 0.1$ T), whereas a saturation is found for higher applied fields. In Figure 3(c), the corresponding values for the magnetic correlation function ξ are shown. As ξ probes the product of the correlation length and the average variation in magnetic induction $\langle\left|\Delta\vec{B}(\vec{r})\right|^2\rangle$, a more disordered magnetic configuration present at small applied fields (as shown in Figure 2(b)) results in a bigger value of ξ. Figure 3(d) compares δ_{ND} to δ_s. A very good consistency is found for the whole range of applied fields, although a small but growing deviation is found for increasing values of $\sigma/\langle R\rangle$.

4.2. Influence of the volume fraction

Figure 4 shows the characteristic 3DND parameters as a function of the applied field for different magnetic fractions f with a constant relative distribution width of $\sigma/\langle R\rangle = 0.25$. It can be seen from Figure 4(a) that the value of f indeed has a significant effect on the rotation angle φ as the saturation level roughly scales with the magnetic fraction. Similarly, the saturation level of $\det(\hat{D})$ is very sensitive to the magnetic fraction (see Figure 4(b)) in comparison with the effect of varying $\sigma/\langle R\rangle$ (see Figure 3(b)). It is interesting to note that for $f = 0.05$, the derived $\det(\hat{D})$

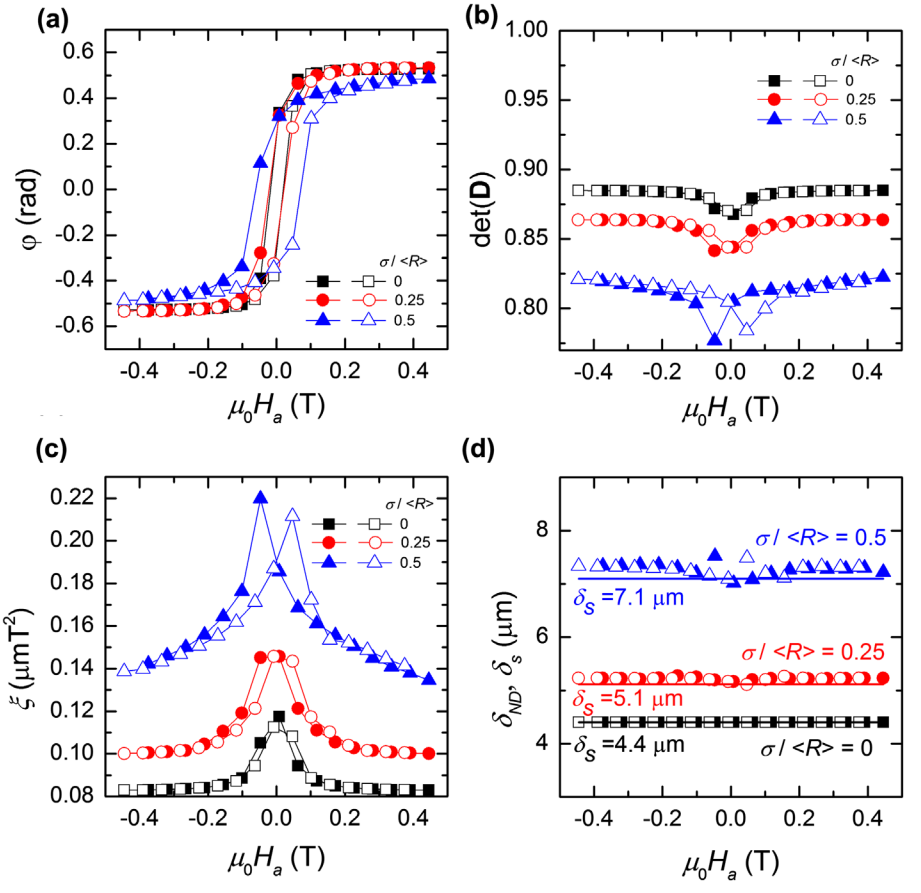

Figure 3. (colour online) Derived 3DND parameters as a function of the applied field $\mu_0 H_a$ for microstructures with a constant magnetic fraction $f = 0.10$ and different values of the distribution width $\sigma\langle R\rangle$: (a) rotation angle φ, (b) determinant of depolarisation matrix $\hat{D}$, (c) correlation function ξ and (d) average particle radius δ_{ND}. In (d), the average particle radius δ_s calculated directly from the microstructures computationally generated is plotted as solid lines.
Notes: The relevant particle size characteristics are indicated in each figure. Note that the closed symbols correspond to a decreasing applied magnetic field, while the open symbols correspond to an increasing applied magnetic field.

shows a negligible dependence on the applied field. However, the sensitivity of $\det(\hat{D})$ to the applied magnetic field increases significantly for increasing values of f. For increasing values of f, the difference between δ_{ND} and δ_s becomes more pronounced. At small applied fields, δ_{ND} underestimate δ_s, whereas at higher fields δ_{ND} is larger than δ_s.

Similar results for ξ as a function of applied field are found for a value of constant σ/R (Figure 4(c)) and a constant value of f (Figure 3(c)). As the magnetic fraction f increases, the effect of magnetic inter-particle interactions becomes more pronounced, resulting in an increasing hysteresis.

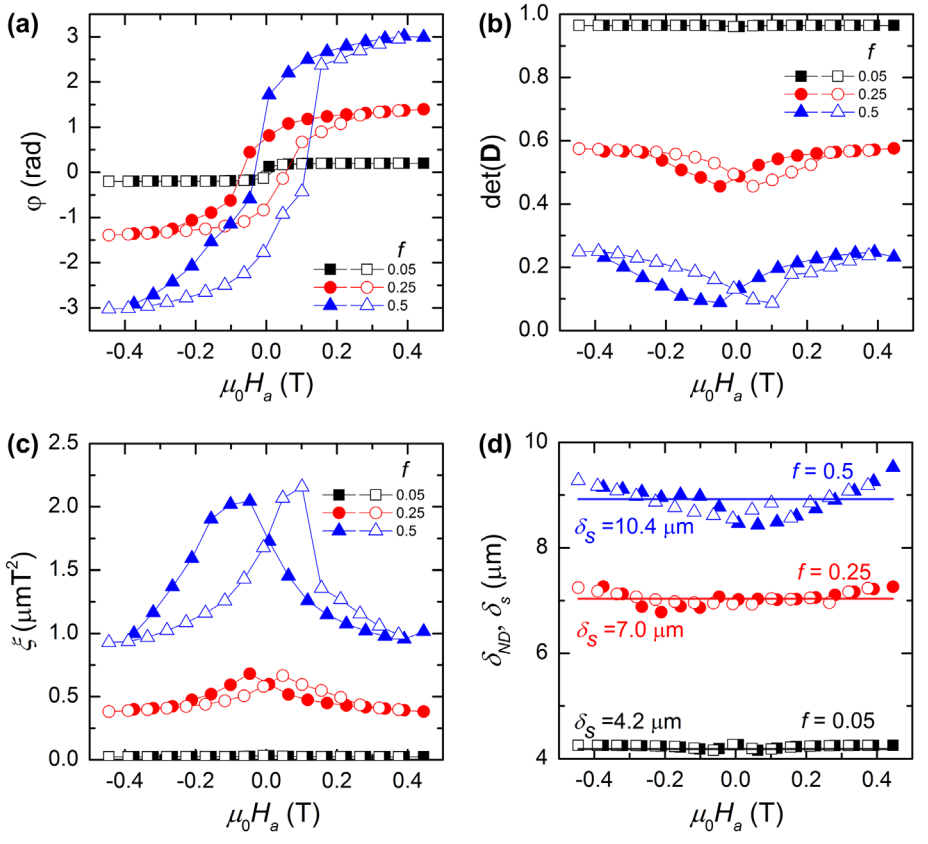

Figure 4. (colour online) Derived 3DND parameters as a function of the applied field $\mu_0 H_a$ for microstructures with a constant $\sigma\langle R\rangle = 0.25$ and different values of the magnetic fraction f: (a) rotation angle φ, (b) determinant of depolarisation matrix $\hat{D}$, (c) correlation function ξ and (d) average particle radius δ_{ND}. For comparison in (d), the average particle radius δ_s calculated directly from the microstructure is shown as solid lines.

Notes: The values are indicated in the figure. Note that the closed symbols correspond to a decreasing applied magnetic field, while the open symbols correspond to an increasing applied magnetic field.

4.3. Determination of the particle size

The simulations of Figures 3 and 5 show that an increase in the width of the particle size distribution enhances the difference between δ_{ND} and δ_s. The main reason for this difference is that magnetic correlations were assumed to be negligible when Equations (5)–(9) were derived. However, in the present numerical calculations, these magnetic correlations are explicitly included. In addition, parameter $c_3 = 16/\left[9\left(1+\langle m_x^2\rangle\right)\right]$ in Equations (8) and (9) has been derived for identical spheres, but was applied for poly-dispersed spheres.

In Figure 5, a comparison between δ_{ND} and δ_s as a function of f is made for different values of $\sigma/\langle R\rangle$ at applied magnetic fields ranging from −0.39 to + 0.39 T. In general, δ_{ND} is in good agreement with δ_s over the range of magnetic fractions and size distributions studied. However, the difference increases with increasing f

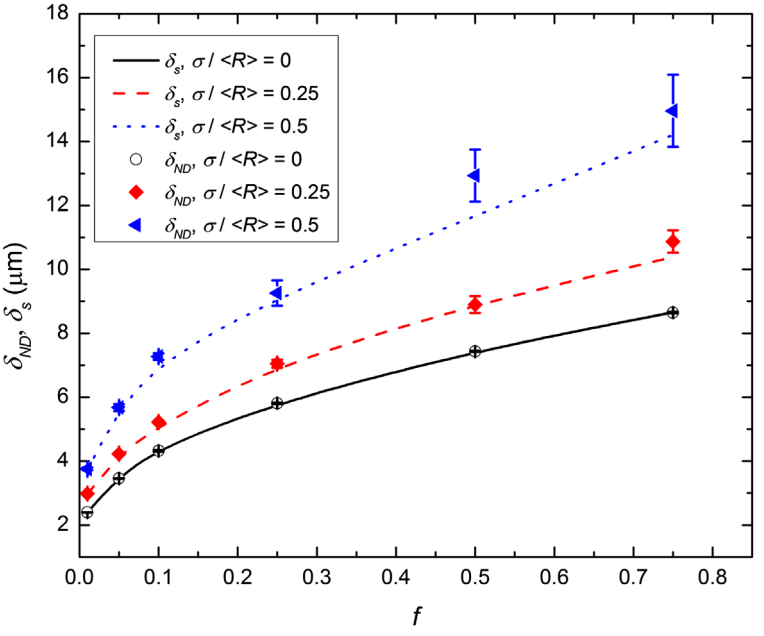

Figure 5. (colour online) Comparison between the particles radius δ_{ND} derived by an 3DND analysis and the actual particle radius δ_s for different size distributions with $\sigma\langle R\rangle = 0$, 0.25 and 0.50 as a function of the magnetic fraction f at applied fields ranging from −0.39 to +0.39 T.

and $\sigma/\langle R\rangle$. As explained earlier, this difference is mainly attributed to the limited validity of the assumptions made in the original 3DND analysis. As can be seen in Figure 5, the maximum difference between δ_{ND} and δ_s is about 13%, which is satisfactory for most experiments. Based on this analysis, it was possible to deduce the number density ρ of magnetic particles. A simple relation based on the assumption of identical spherical particles yields $\rho = 3f/4\pi\delta^3$ with an estimated number density that is found to be within a factor 5 compared to the real magnetic particle number density.

To accurately determine the average particle size, an accurate relationship between ξ and δ is required. Te Velthuis and co-workers [12] analysed the dependence of ξ on the magnetic configuration. They generalised Equation (8) as:

$$\xi = \delta f \left(\mu_0 M_s\right)^2 \left(a_1\left(1 + \langle m_x^2\rangle\right) - a_2 m^2\right) \tag{13}$$

In the previous analysis, the constants were equal to $a_1 = 3/4$ and $a_2 = 4/3(4\pi f^2/81)$. In their numerical study, it was found that the parameters a_1 and a_2 were sensitive to (1) the ferrite grain size distribution and (2) the spatial homogeneity of the ferrite grains.

Since the analytical solution of Equation (4) was derived for mono-disperse particle distributions, it is not straightforward to include the effect of the size distribution on ξ. An alternative approach is to compare the numerical results for

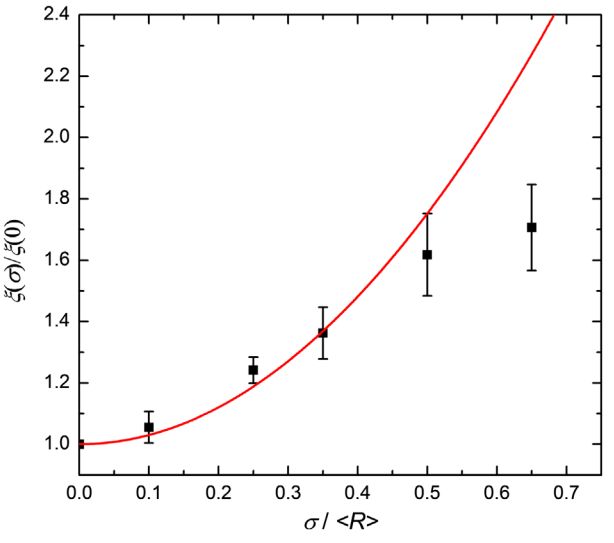

Figure 6. (colour online) Normalised field correlation function $\xi(\sigma)/\xi(0)$ as a function of $\sigma\langle R\rangle$. The solid line shows the fit to the relationship $\frac{\xi(\sigma)}{\xi(0)} = 1 + 3.0(3)\left(\frac{\sigma}{\langle R\rangle}\right)^2$ for $\sigma\langle R\rangle \leq 0.5$.

poly-disperse particle distributions to those for identical particles to investigate its influence. To this aim, we calculated the ratio of $\xi(\sigma)/\xi(0)$ for different values of f. The results show that $\xi(\sigma)/\xi(0)$ is nearly independent of both the applied field and the magnetic fraction f at a fixed value of σ/R. However, $\xi(\sigma)/\xi(0)$ increases with increasing σ/R. When we plot the parameter $\xi(\sigma)/\xi(0)$ as a function of $\sigma/\langle R\rangle$, as shown in Figure 6, a power law dependence $\frac{\xi(\sigma)}{\xi(0)} - 1 \propto \left(\frac{\sigma}{R}\right)^p$ with $p = 2$ is observed for $\sigma/\langle R\rangle \leq 0.5$. This relation suggests that the effect of the size distribution on ξ can be described by an additional factor. We can therefore conclude that the relation

$$\frac{\xi(\sigma)}{\xi(0)} = 1 + \chi\left(\frac{\sigma}{R}\right)^2 \tag{14}$$

with $\chi = 3.0(3)$ can be used to describe the correlation function for poly-disperse particle size distributions. The variable $\xi(0)$ can be calculated with Equation (8). The newly derived equation (14) is now a very useful addition to analyse experimental 3DND data. For an identical particle system (mono-disperse), the average particle size can be calculated with Equation (9). For a poly-disperse system, $\xi(\sigma > 0)$ can be expressed as a function of $\sigma/\langle R\rangle$ with Equation (14), as shown in Figure 6. The effective size δ can then be calculated with Equation (9). Since δ now directly depends on $\sigma/\langle R\rangle$, the additional relation of Equation (14) provides an accurate estimate for δ. For a lognormal distribution $f(R) = \frac{1}{R\omega\sqrt{2\pi}}\exp\left(-\frac{(\ln(R)-\mu)^2}{2\omega^2}\right)$, one can derive the moments of the radius $\langle R^n\rangle = \exp\left(n\mu + n^2\omega^2/2\right)$ and $\omega^2 = ln\left(1 + \left(\frac{\sigma}{\langle R\rangle}\right)^2\right)$. Combining these relations yields $\frac{\langle R^4\rangle}{\langle R^3\rangle\langle R\rangle} = \left(1 + \frac{\sigma^2}{\langle R^2\rangle}\right)^3$.

For $\sigma/R \ll 1$, this results in $\frac{\langle R^4\rangle}{\langle R^3\rangle\langle R\rangle} \approx 1 + 3\left(\frac{\sigma}{\langle R\rangle}\right)^2$, which is fully consistent with the fitted relationship shown in Figure 6. Hence, the relationship between $\xi(\sigma)/\xi(0)$ and σ/R found in the present study is suitable to determine both the particle size and the width of the size distribution, particularly for $\sigma/R \leq 0.5$. The average particle size now corresponds to $\langle R\rangle \approx \frac{\delta}{1+3(\sigma/\langle R\rangle)^2}$.

In the above simulations, the value of σ/R is set as a constant. During the austenite-to-ferrite phase transformations in steels, σ/R is found to vary between 0 and 0.7 [14,28], but once nucleation is completed σ/R tends to fluctuate around a constant value. This behaviour simplifies the above 3DND analysis to obtain a reliable experimental estimate of the magnetic particle size (ferrite grain size) and size distribution during phase transformations in steels. The newly established relationship between $\xi(\sigma > 0)$ and $\xi(\sigma = 0)$ thereby sheds new light on the analysis of size distributions of magnetic particles from the 3DND data. It should be noted that the geometry of the ferrite particles has been simplified in the present modelling to a spherical shape. Under most conditions, the simplified geometry used here reflects the ferrite growth reasonably well in the initial stages of the transformation. The conclusions drawn from this study are thereby very useful to link the 3DND parameters to the microstructural characteristics.

5. Conclusions

We have computed magnetic configurations for magnetic microstructures with mono- and poly-disperse magnetic particles in 3D space and translated those to the characteristic 3DND parameters. The correlation function and the determinant of the depolarisation matrix are found to be very sensitive not only on the magnetic phase fraction and average particle size, but also on the particle size distribution. The correlation function increases with increasing volume fractions and with the width of the particle size distribution of the magnetic particles. The magnetic particle size derived from 3DND data is found to be in very good agreement with the computed microstructural particle size over a wide range of volume fractions and grain size distributions. Deviations in the estimated particle size from 3DND data are found to originate from the spread in particle size. A relationship between the field correlation function and the relative width of the particle size distribution is found that accurately describes the deviations. The present simulations shed new light on the analysis of 3DND data from magnetic particle systems with a poly-disperse particle size distribution and are extremely useful to deepen the analysis of the austenite–ferrite transformation in low-alloyed steels.

Acknowledgements

The authors appreciate many clarifying discussions with Dr Theo Rekveldt. Haixing Fang is grateful to the financial support provided by the China Scholarship Council (CSC).

Disclosure statement

No potential conflict of interest was reported by the authors.

References

[1] R. Rosman and M.T. Rekveldt, *Neutron-depolarization theory in particulate media*, Phys. Rev. B 43 (1991), pp. 8437–8449.
[2] M.T. Rekveldt, N.H. van Dijk, S.V. Grigoriev, and W.G. Bouwman, *Three-dimensional magnetic spin-echo small-angle neutron scattering and neutron depolarization: A comparison*, Rev. Sci. Instr. 77 (2006), pp. 073902.
[3] A. Kumar, *Magnetic correlations at domain/cluster length scales using neutron depolarization*, Proceedings of the sixth conference on neutron scattering, 21–23 Nov. 2016, Mumbai, India.
[4] M.T. Rekveldt and F.J. van Schaik, *Static and dynamic neutron depolarization studies of ferromagnetic domain structures*, J. Appl. Phys. 50 (1979), pp. 2122–2127.
[5] S. Mitsuda and Y. Endoh, Neutron depolarization studies on magnetization process using pulsed polarized neutrons, J. Phys. Soc. Jpn. 54 (1985), pp. 1570–1580.
[6] I. Mirebeau, S. Itoh, S. Mitsuda, T. Watanabe, Y. Endoh, M. Hennion, and R. Papoular, *Neutron depolarization in a reentrant spin-glass system: Amorphous Fe-Mn*, Phys. Rev. B 41 (1990), pp. 11405–11416.
[7] R. Rosman and M.T. Rekveldt, *Neutron depolarization in particulate media: A review of theory and experimental results*, J. Magn. Magn. Mater. 95 (1991), pp. 319–340.
[8] Ö. Çakr, M. Acet, M. Farle, and A. Wilders, *Magnetic correlations in the magnetocaloric materials Mn_3GaC and $Mn_3GaC_{0.85}N_{0.15}$ studied by neutron polarization analysis and neutron depolarization*, J. Phys. Condens. Matter. 28 (2016), p. 13LT02.
[9] K. Manna, D. Samal, A.K. Bera, S. Elizabeth, S.M. Yusuf, and P.S. Anil, *Kumar, Correspondence between neutron depolarization and higher order magnetic susceptibility to investigate ferromagnetic clusters in phase separated systems*, J. Phys. Condens. Matter 26 (2013), p. 016002.
[10] S.G.E. te Velthuis, N.H. van Dijk, MTh Rekveldt, J. Sietsma, and S. van der Zwaag, *Field-dependent neutron depolarization of the ferrite formation in medium-carbon steels*, Acta Mater. 48 (2000), pp. 1105–1114.
[11] S.E. Offerman, L.J.G.W. van Wilderen, N.H. van Dijk, M.Th. Rekveldt, J. Sietsma, and S. van der Zwaag, *In-situ study of pearlite nucleation and growth during the isothermal austenite decomposition in nearly eutectoid steel*, Acta Mater. 51 (2003), pp. 3927–3938.
[12] S.G.E. te Velthuis, N.H. van Dijk, M.T. Rekveldt, J. Sietsma, and S. van der Zwaag, *Domain size determination of granular ferromagnetic systems with neutron depolarization*, J. Appl. Phys. 89 (2001), pp. 1275–1280.
[13] R. Rosman and M.T. Rekveldt, *Neutron depolarization theory in the Larmor and the scattering approach*, Z. Phys. B Condens. Matter 79 (1990), pp. 61–68.
[14] H. Fang, M.G. Mecozzi, E. Brück, S. van der Zwaag, and N.H. van Dijk, Analysis of the grain size evolution for ferrite formation in Fe-C-Mn steels using a 3D model under a mixed-mode interface condition, Metall. Mat. Trans. A 49 (2018), pp. 41–53.

[15] M. Enomoto and H.I. Aaronson, *Nucleation kinetics of proeutectoid ferrite at austenite grain boundaries in Fe-C-X alloys*, Metall. Mater. Trans. A 17 (1986), pp. 1385–1397.
[16] W. Huang and M. Hillert, *The role of grain corners in nucleation*, Metall. Mater. Trans. A 27 (1996), pp. 480–483.
[17] M. Militzer, R. Pandi, and E.B. Hawbolt, *Ferrite nucleation and growth during continuous cooling*, Metall. Mater. Trans. A 27 (1996), pp. 1547–1556.
[18] E. Gamsjäger, M. Militzer, F. Fazeli, J. Svoboda, and F.D. Fischer, *Interface mobility in case of the austenite-to-ferrite phase transformation*, Comp. Mater. Sci. 37 (2006), pp. 94–100.
[19] E. Gamsjäger, R.E. Werner, W. Schiller, and B. Buchmayr, Kinetics of the austenite-to-ferrite phase transformation – Simulations and experiments, Steel Res. Int. 85 (2014), pp. 131–142.
[20] E. Gamsjäger, M. Wiessner, S. Schider, H. Chen, and S. van der Zwaag, *Analysis of the mobility of migrating austenite-ferrite interfaces*, Philos. Mag. 95 (2015), pp. 2899–2917.
[21] Y.J. Lan, D.Z. Li, and Y.Y. Li, *Modeling austenite decomposition into ferrite at different cooling rate in low-carbon steel with cellular automaton method*, Acta Mater. 52 (2004), pp. 1721–1729.
[22] M. Militzer, M.G. Mecozzi, J. Sietsma, and S. van der Zwaag, *Three-dimensional phase field modelling of the austenite-to-ferrite transformation*, Acta Mater. 54 (2006), pp. 3961–3972.
[23] E.C. Stoner and E.P. Wohlfarth, A Mechanism of magnetic hysteresis in heterogeneous alloys, Philos. Trans. R. Soc. London Ser. A 240 (1948), pp. 599–642.
[24] D.C. Jiles and D.L. Atherton, *Theory of ferromagnetic hysteresis*, J. Magn. Magn. Mater. 61 (1986), pp. 48–60.
[25] J.D. Jackson, *Classical electrodynamics*, 3rd ed., Wiley, New York, 1999.
[26] B.F. Phelps, F. Liorzou, and D.L. Atherton, *Inclusive model of ferromagnetic hysteresis*, IEEE Trans. Magn. 38 (2002), pp. 1326–1332.
[27] A.S. Arrott and B. Heinrich, *Application of magnetization measurements in iron to high temperature thermometry*, J. Appl. Phys. 52 (1981), pp. 2113–2115.
[28] M.G. Mecozzi, M. Militzer, J. Sietsma, and S. van der Zwaag, The role of nucleation behavior in phase-field simulations of the austenite to ferrite transformation, Metall. Mater. Trans. A 39 (2008), pp. 1237–1247.